




Time-dependent sorption behavior of lentiviral vectors during anion-exchange chromatography

George Pamenter^{1,2}  | Lee Davies² | Carol Knevelman² | James Miskin² | Kyriacos Mitrophanous² | Duygu Dikicioglu¹  | Daniel G. Bracewell¹ 

¹Department of Biochemical Engineering, University College London, London, UK

²Oxford Biomedica (UK) Ltd, Oxford, UK

Correspondence

Daniel G. Bracewell, Department of Biochemical Engineering, University College London, London, UK.
Email: d.bracewell@ucl.ac.uk

Funding information

Oxford Biomedica (UK) Ltd.

Abstract

Use of lentiviral vectors (LVs) in clinical Cell and Gene Therapy applications is growing. However, functional product loss during capture chromatography, typically anion-exchange (AIEX), remains a significant unresolved challenge for the design of economic processes. Despite AIEX's extensive use, variable performance and generally low recovery is reported. This poor understanding of product loss mechanisms highlights a significant gap in our knowledge of LV adsorption and other types of vector delivery systems. This work demonstrates HIV-1-LV recovery over quaternary-amine membrane adsorbents is a function of time in the adsorbed state. Kinetic data for product loss in the column bound state was generated. Fitting a second order-like rate model, we observed a rapid drop in functional recovery due to increased irreversible binding for vectors encoding two separate transgenes ($t_{Y_{1/2}} = 12.7$ and 18.7 min). Upon gradient elution, a two-peak elution profile implicating the presence of two distinct binding subpopulations is observed. Characterizing the loss kinetics of these two subpopulations showed a higher rate of vector loss in the weaker binding peak. This work highlights time spent in the adsorbed state as a critical factor impacting LV product loss and the need for consideration in LV AIEX process development workflows.

KEYWORDS

capture chromatography, Cell and Gene Therapy, downstream processing, lentiviral purification, lentivirus, viral vector

1 | INTRODUCTION

In recent years treatment of disease by means of Cell and Gene Therapy (C>) has gone from concept to commercial reality with 2093 clinical trials ongoing globally in 2022 (Alliance for Regenerative Medicine, 2022). This has largely been driven by advances in manufacturing of clinical-grade viral vectors (Bulcha et al., 2021).

Lentiviral vectors (LVs) are a particularly promising product class due to their ability to stably deliver large genetic payloads (up to ~10 kb) to both dividing and nondividing cells (Lewis et al., 1992; Mátrai et al., 2010; Naldini et al., 1996). These factors make lentiviruses the vector of choice for cell therapies, particularly Chimeric Antigen Receptor T-cell (CAR-T) therapies for treatment of various leukemias and lymphomas (National Cancer Institute, National Institutes of

This is an open access article under the terms of the Creative Commons Attribution License, which permits use, distribution and reproduction in any medium, provided the original work is properly cited.

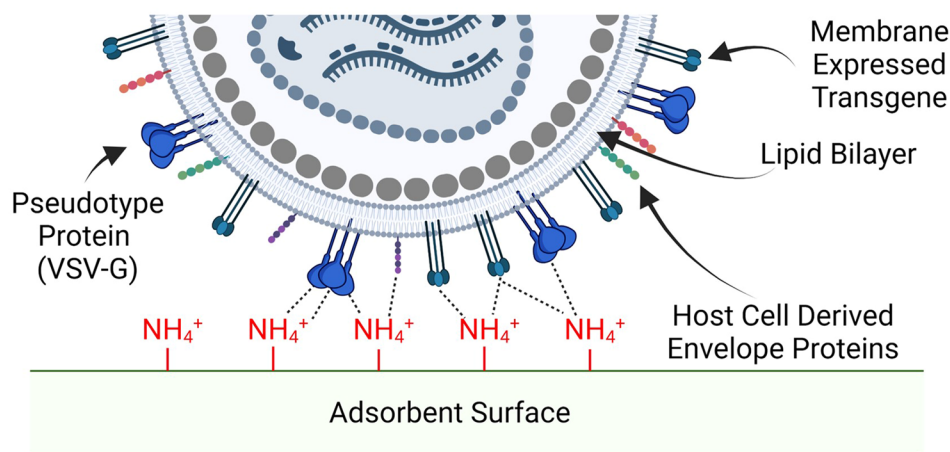
© 2023 The Authors. *Biotechnology and Bioengineering* published by Wiley Periodicals LLC.

Health, 2022). Further interest has been driven by the recent FDA approval of LV-based products such as Kymriah[®] (Novartis), Carvytki[™] (Janssen Biotech), and Zynteglo[®] (Bluebird Bio) demonstrating the therapeutic potential of this vector class (FDA, 2021, 2022a, 2022b). As a result, LVs are a key contributor in C> markets, accounting for 48% ($n = 235$) of current known gene therapy and cell-based Immuno-oncology trials globally and 66% of the United Kingdom ex vivo C> clinical trials in 2022 (Alliance for Regenerative Medicine, 2022; Cell and Gene Therapy Catapult, 2022). Despite these initial successes LV therapies still have huge potential for further utilization and future commercial successes. Increased use in vivo and targeting of larger and less severe

disease indications will likely drive demand for greater quantity of product that is subject to heightened regulatory stringency (Glover, 2021).

The predominant LV of choice for clinical applications is based on Human Immunodeficiency Virus Type 1 (HIV-1) (Merten et al., 2016). HIV-1 is a spherical (80–120 nm) ssRNA virus whose genome is encapsulated in a p24 protein core enveloped in a lipid bilayer studded with a variety of proteins derived from the production cell membrane upon budding (Figure 1a) (King, 1994; Nguyen & Hildreth, 2000). Because of this structural complexity, in particular, due to the enveloped nature of the particles, efficient, reliable purification of LVs remains a challenge for large-scale vector

(a) Interaction interface of lentiviral vector and AIEX adsorbent



(b) Schematic of potential lentiviral vector AIEX adsorption kinetics

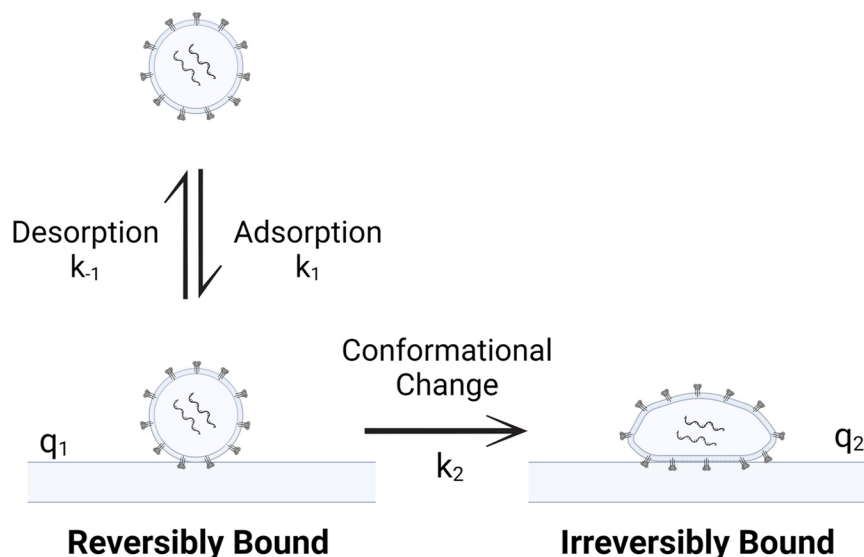


FIGURE 1 Schematic of suggested mechanism of LV binding on AIEX adsorbents. (a) Interaction interface of LV and anion-exchange ligands indicating multipoint attachment of envelope proteins. (b) Schematic of proposed LV adsorption mechanism indicating the binding and subsequent conformational change in LV to the irreversibly bound state with q_1 and q_2 representing the “reversibly” bound and “irreversibly” bound states, respectively. k_2 denotes the rate constant of conformational change. LV, lentiviral vector.

production due to the loss of product and infectivity during downstream processing. Typically, product capture relies on the use of convective anion-exchange (AIEX) adsorbents such as membranes and monoliths which were not initially designed for viral purification. Although AIEX is critical to LV bioprocesses and high recoveries have been reported (Bandeira et al., 2012; Ruscic et al., 2019), ~30%–40% functional vector recovery is not uncommon for large-scale AIEX applications with a variety of adsorbent types, chemistries, and physiochemical conditions reported in the literature (Ghosh et al., 2022; Moreira et al., 2021; Valkama et al., 2020). The inconsistent and generally low recoveries reported for LV AIEX likely stem from a poor understanding of the critical factors that determine adsorption and product loss, as well as the role key vector structural components play in binding. This emphasizes the need to further elucidate LV adsorption phenomena, which in turn will pave the way for rational design of this process step.

Typical mechanistic descriptions for binding of larger biological products to AIEX adsorbents rely on variations of the Steric Mass Action (SMA) model, which considers the impact of salt ions, biomolecule binding strength, and steric hinderance (Effio et al., 2016; Vicente et al., 2008, 2011). The SMA model also assumes no structural changes in the bound state occur. More complex AIEX isotherms accounting for different binding states have however been suggested for protein systems (Diedrich et al., 2017). Thus, the perception that viral particles of all types are a homogenous target existing in a relatively stable and unchanging bound form is likely an oversimplification of the adsorption process, particularly when considering the large size, molecular complexity, and enveloped nature of LVs. Valkama et al., 2020 previously described a failure to elute more than “30% of column-bound functional LVs” using up to 1.5 M NaCl. This partial recovery of vector could stem from changes in binding strength due to rearrangement in the adsorbed state or from a level of product heterogeneity with subpopulations of LV possessing differing interaction strengths.

Charge heterogeneity of VSV-G pseudotyped LV has been previously observed with gradient elution on strong anion-exchangers demonstrating a two-peak profile (Yamada et al., 2003). Typically, two-peak elution profiles for other viral vectors such as Adeno-Associated Virus (AAV) result from the presence of empty and full vector particles (Khatwani et al., 2021; Urabe et al., 2006). However, Yamada et al. (2003) demonstrated that upon omission of the vector transgene construct during production, the same two-peak elution profile was observed. Poor understanding of the causes behind these phenomena highlights a considerable gap in our understanding of LV sorption behavior.

Load time and flowrates are often not considered in viral vector AIEX due to the assumed lack of diffusional mass transfer resistance in the membrane or monolith typically used or that, in classical porous bead-based chromatography, only the surface of a bead is accessible due to the small bead pore size restricting virus access (Orr et al., 2013). However, time-dependent recoveries have been reported in these systems (Turnbull et al., 2019). In the solid phase materials used, cellulose nanofibers, Turnbull et al. (2019)

demonstrated that extended durations of time in the adsorbed state on quaternary-amine (Q) Nanofiber modalities reduced the recovery of functional Adenovirus 5 (Ad5) and showed that this impact could be mitigated by lowering multipoint attachment through reduced adsorbent ligand densities. Similar ligand density effects were also observed during AIEX purification of recombinant hepatitis B surface antigen particles (Huang et al., 2006). This behavior could be explained utilizing the theory used to explain other chromatographic systems in which time-dependent recovery of bound material is observed. These include protein systems during Hydrophobic Interaction Chromatography (HIC) (Haimer et al., 2007; Jungbauer et al., 2005; Ueberbacher et al., 2008). Here loss of material is attributed to increased irreversible binding at prolonged adsorption times due to strengthening hydrophobic interactions as the protein is “spread” over the adsorbent. The rate of product loss, defined by the Langmuir-spreading model, is dependent on the proteins rigidity, binding strength, and the free surface available (Ueberbacher et al., 2008). Similar observations were also made during adsorption of bovine serum albumin (BSA) on multimodal AIEX resins (Roberts & Carta, 2022). Here, loss of recoverable material with time was attributed to an increase in irreversibly bound species that result from aggregation of BSA into higher order oligomers. The effect was most pronounced in conditions leading to high binding strength (high pH, low salt) and at high temperature. Comparable phenomena may therefore be present during viral vector adsorption in AIEX.

This work aims to investigate the relationship between time spent in the adsorbed state and LV product loss on AIEX adsorbents. We hypothesized a potential mechanism (Figure 1) and measured the kinetics of functional and total HIV-1 vector particle recovery, comparing the kinetic profiles of a model HIV-1-GFP vector and a clinical vector encoding a chimeric antigen receptor (HIV-1-CAR). Finally, we characterized the impact of product heterogeneity by measuring adsorption time effects on subpopulations of eluted LV from linear gradient elution profiles.

2 | MATERIALS AND METHODS

2.1 | Cell culture and clarification

Third-generation HIV-1 LVs were generated following multi-plasmid co-transfection of the suspension adapted HEK293T 1.65 s cell line (Oxford Biomedica). Briefly, cells were inoculated at approximately 1×10^6 cells/mL in serum-free FreeStyle 293 Expression Media (Thermo Fisher Scientific) in glass stirred tank bioreactors (STRs) (Applikon) and agitated using an impeller stirring rate of 290 rpm. Cells were incubated at a temperature of 37°C, a pH set point of 7.2 and dissolved oxygen was maintained in excess of 20% throughout using an air/oxygen mix supplied via a sintered bead porous sparger. LV production was instigated via transient co-transfection of cells with four viral production plasmids. pOXB-GP (gag-pol protein and viral enzymatic components), pOXB-Rev, pOXB-VSV-G, and pOXB-GFP/CAR (transgenes) complexed to the

transfection reagent Lipofectamine™ 2000CD (Thermo Fisher Scientific) in accordance with manufacturer's guidelines. Approximately 24 h before vector harvest, LV production was stimulated by supplementation of the bioreactor contents with the histone deacetylase inhibitor sodium butyrate (Sigma-Aldrich, Merck). At the termination of the production phase, bioreactor contents were clarified using a 0.2 µm normal flow filter (Pall Corporation) operating at 50 LMH. Clarified vector was stored at -80°C before use in chromatography studies.

For all HIV-1-GFP contact time experiments, material was derived from two separate STRs operated under the same conditions. HIV-1-GFP material derived from the first bioreactor source (GFP1) was used for initial testing at different mobile phases (Figure 2) and for kinetic analysis (Figure 3). The second HIV-1-GFP bioreactor material (GFP2) was used for the contact time gradient elution analysis (Figure 5). For HIV-1-CAR, material was derived from a single STR source (CAR).

2.2 | Anion-exchange chromatography

For each study frozen vector material was rapidly thawed at 37°C in a water bath. AIEC was conducted using an ÄKTA Avant 150 (Cytiva) and Sartobind® Q nano 1 mL membrane adsorber (Sartorius). Three chromatography buffers were used. All buffers were formulated with 20 mM Tris, pH 7.2 and varying NaCl concentrations (Buffer A = 150 mM, Buffer B = 2000 mM, Buffer C = 1200 mM). Before processing ÄKTA systems and membranes units were subject to a decontamination in 0.5 M NaOH. Finally, Sartobind® Q membranes were charged with Buffer B then equilibrated in Buffer A.

Isocratic elutions were conducted using Buffer C. For gradient elution, the linear salt increase was achieved by mixing Buffer A and B up to 64.9% Buffer B content (1350 mM NaCl). The salt composition of each fraction was determined by measuring conductivity offline on the Orion Star™ A211 Benchtop pH/Conductivity Meter (Thermo Fisher Scientific).

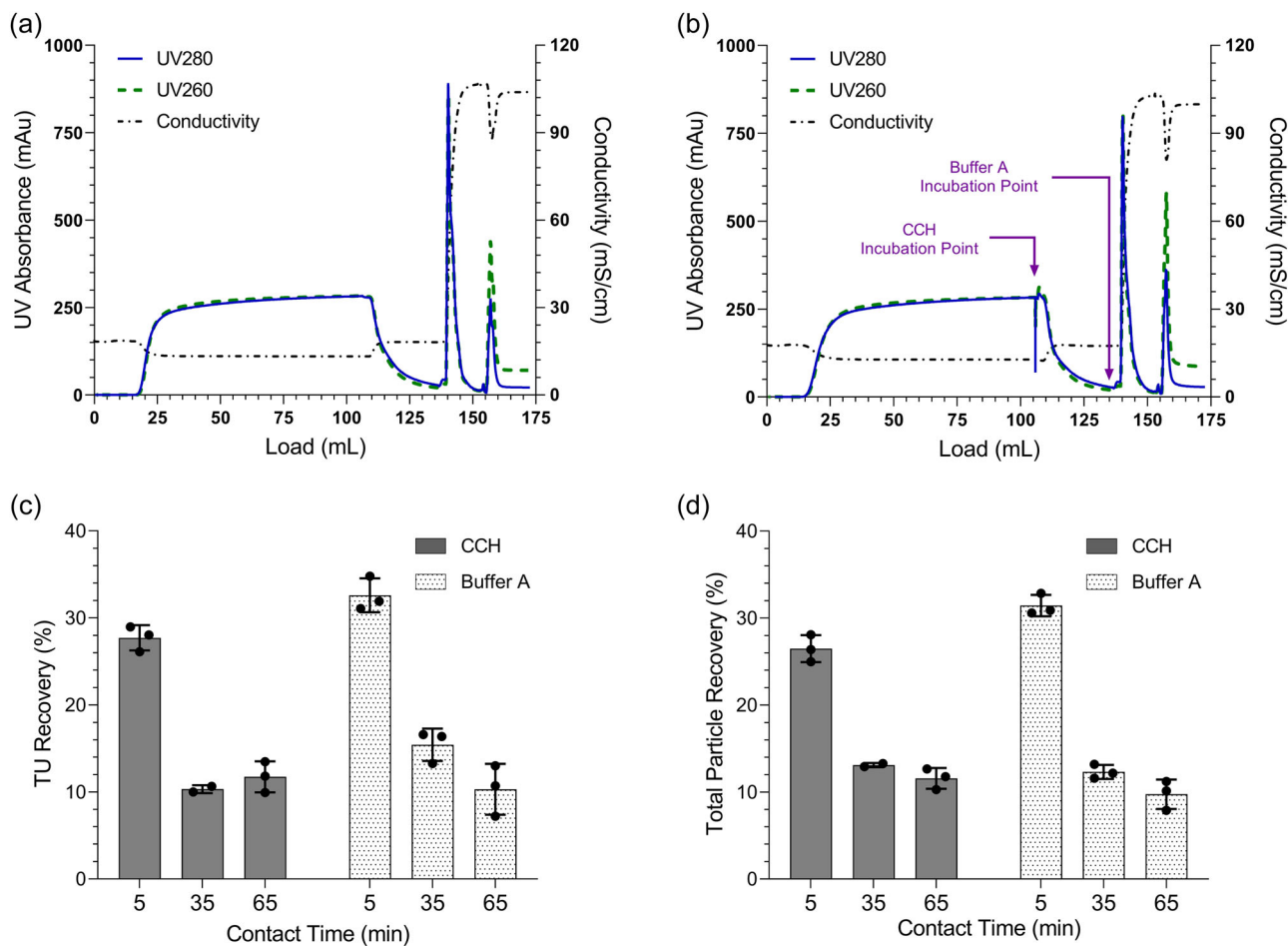


FIGURE 2 Impact of adsorbed contact time on recovery of functional vector and total particles. (a) Representative AIEC chromatogram for 5 min adsorption time. Chromatogram displays the 95 mL load of clarified Cell Culture Harvest (CCH) followed by 30 mL Buffer A wash. Peak 1 represents 1.2 M NaCl elution and Peak 2 the 0.5 M NaOH strip (b) Representative AIEC chromatogram for 65 min adsorption time. Incubation hold points are indicated on the chromatogram by purple arrows. (c) Functional titer recovery (TU %) for CCH and Buffer A contacting mobile phases. (d) Total particle recovery (p24%) for CCH and Buffer A contacting mobile phases.

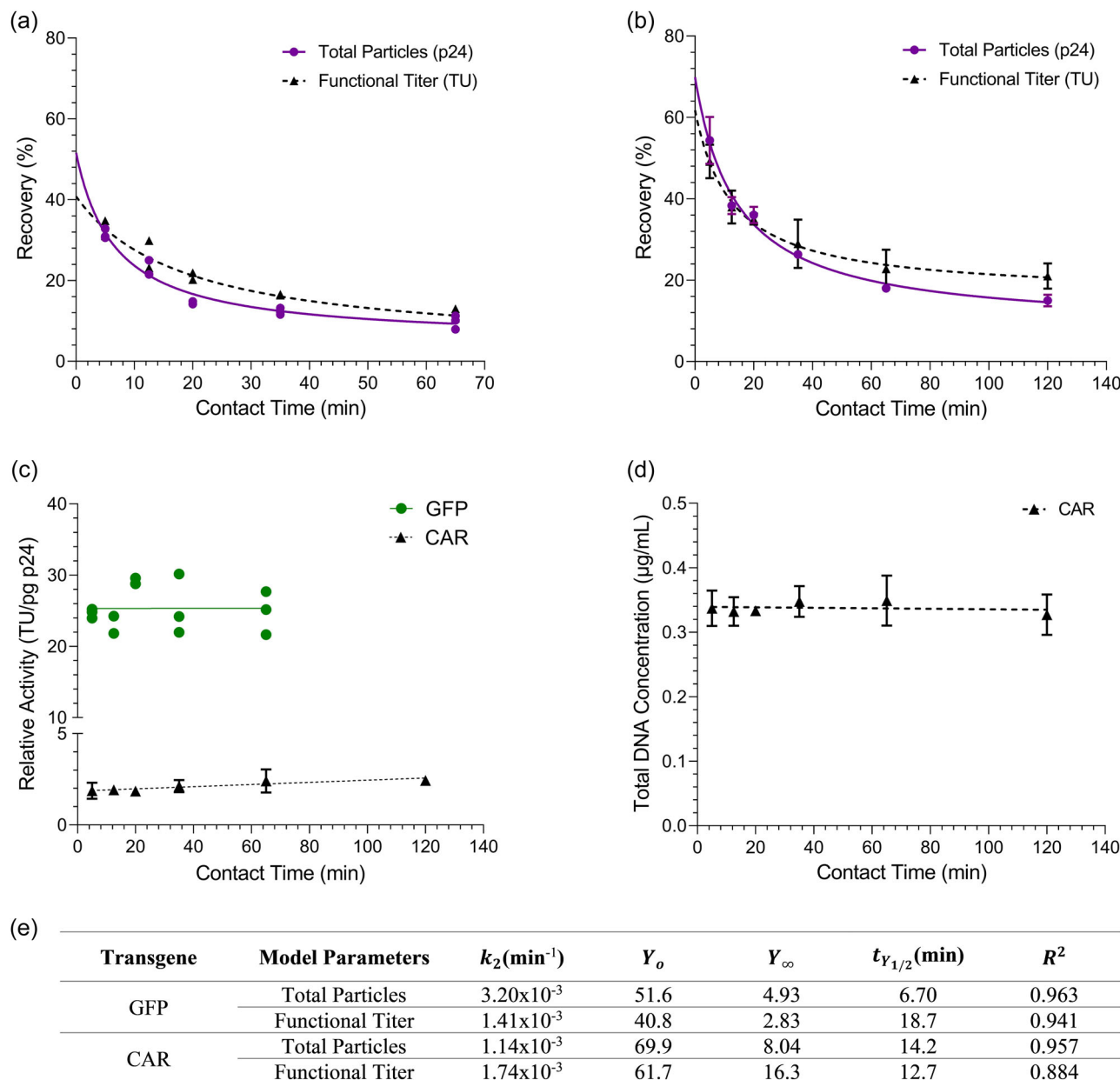


FIGURE 3 Kinetic analysis of HIV-1-GFP and HIV-1-CAR vector recovery and activity. Individual runs are given for GFP1. For CAR error bars represent ± 1 SD at $N = 3$ biological replicates (a) Effect of time spent in the adsorbed state on HIV-1-GFP1 LV recovery. (b) Effect of time spent in the adsorbed state on HIV-1-CAR LV recovery. (c) Effect of time spent in the adsorbed state on the relative activity of eluted HIV-1-GFP1 and HIV-1-CAR. It should be noted that Chauvenet's criterion was used for statistical rejection of outliers at $p = 0.05$ leading to the elimination of a data point for the CAR transgene construct at $t = 140$ min. (d) Impact of time spent in the adsorbed state on eluted concentration of total DNA from HIV-1-CAR material. (e) Model fit parameters for HIV-1-GFP and HIV-1-CAR kinetic profiles.

For isocratic elution 95 column volumes (CV) of thawed clarified cell culture harvest (CCH) was loaded directly to a 1 mL Sartobind® Q Nano (Sartorius) at 65 CV/min. Load was followed by a 30 CV Buffer A wash at 65 CV/min to flush CCH from the system hold up. In isocratic mode the product was eluted using 15 CV of Buffer C. Eluted material was collected in 45 mL of 20 mM Tris solution without NaCl, giving an immediate fourfold dilution of the product peak to 300 mM NaCl. This procedure resulted in an average adsorbed contact time of 5 min. To generate extended time points

an "on-column" static incubation was conducted. For example, 35 min contact time implemented a 30 min static incubation. Incubations were implemented immediately postload or following the postload Buffer A wash (see Figure 2b). Following elution, a 0.5 M NaOH strip was implemented to remove any strongly bound species from the membrane. Gradient elutions (150–1350 mM NaCl) were conducted over 60 CV at a flowrate of 10 CV/min to gain adequate resolution at short contact time. The Buffer A incubation point was used for all gradient experiments, collecting 15 fractions (100 mM Steps).

For nonbinding experiments the exact same loading protocol was used. However, CCH was spiked to 1350 mM NaCl before load. Following load a 40 CV Buffer C wash was conducted to flush material from the system without generating an environment in which residual product might have bound. For determination of the Dynamic Binding Capacity (DBC), 800 CV of CCH was loaded to the Sartobind® Q at 10 CV/min. Fractions were then taken from the flowthrough at 50 CV intervals. The ratio of flowthrough functional titer to loaded CCH titer (C/C_0) was plotted against throughput for each fraction. The first nonzero value for C/C_0 (1%) occurred at 350 CV giving a $DBC_{0\%}$ of 300 CV at this resolution.

2.3 | Functional vector titer measurement

Functional Titer was determined by transduction of adherent HEK293T cells in 12 well plate format. Process samples were first diluted in DMEM Media (Sigma-Aldrich, Merck) and supplemented with polybrene (Sigma-Aldrich, Merck). Each vector preparation was then added to the adherent cells. Samples were analyzed in duplicate or triplicate depending on study design and assay size. Number of target cells on transduction day was determined by NucleoCounter® NC200™ (ChemoMetec). Cells were then harvested, and samples were analyzed on an Attune NxT acoustic focusing flow cytometer (Thermo Fisher Scientific) with GFP fluorescence detected using a 488 nm excitation laser. Size and fluorescence data were collected for 10,000 live events per sample and FlowJo® software used to obtain the percentage of HEK293T cells that exceeded a set fluorescence threshold based on background fluorescence of non-transduced cells. Assuming one transducing unit per transduced cell, GFP titer was calculated using the following equation:

$$\text{Titre} \left(\frac{\text{TU}}{\text{mL}} \right) = \frac{\begin{aligned} & [\% \text{cells expressing GFP} \\ & \times \text{number of cells at transduction} \\ & \times \text{dilution factor}] \end{aligned}}{\text{Volume of Vector added at transduction}} \quad (1)$$

2.4 | p24 concentration and particle size measurement

Total HIV-1 particle measurements were determined by measuring p24 capsid protein concentration using a HIV-1 p24 enzyme-linked immunosorbent assay (ELISA) kit (PerkinElmer). The kit was utilized as per the manufacturer's instructions and plates read using a SpectraMax i3x plate Reader (Molecular Devices) at 490 and 630 nm wavelengths.

Particle size measurements were conducted to test for the presence of LV particles in the AIEX flowthrough. Dynamic Light Scattering (DLS) was used to measure average particle size at 20°C with a Zetasizer Nano (Malvern Scientific) instrument. One hundred microlitres of AIEX flowthrough was loaded onto the instrument with particulate size distributions determined from backscattered light at an angle of 173° using a 633 nm laser.

2.5 | Total vector particle recovery and relative activity calculation

To determine the recovery of total particles over AIEX, p24 concentration was measured. As not all p24 is vector-associated and significant quantities of "free" p24 is present in the AIEX flowthrough, equation [2] was used to calculate total particle recovery.

$$\text{Total particle recovery} = \frac{\text{Eluted p24 mass (pg)}}{\text{Total loaded p24 mass (pg)} - \text{Flowthrough p24 mass (pg)}} \quad (2)$$

The ratio of functional titer to p24 was calculated by equation [3] to determine relative activity of vector material:

$$\text{Relative activity} \left(\frac{\text{TU}}{\text{pg}} \right) = \frac{\text{Functional titre} \left(\frac{\text{TU}}{\text{mL}} \right)}{\text{p24} \left(\frac{\text{pg}}{\text{mL}} \right)} \quad (3)$$

2.6 | Total DNA quantification

Total DNA concentration was determined using the Quant-iT™ PicoGreen® dsDNA kit (Thermo Fisher Scientific). The kit was utilized as per the manufacturer's instructions and plates read using a SpectraMax i3x plate Reader (Molecular Devices).

2.7 | Statistics, nonlinear regression, and model fitting

All statistical analysis (regression and hypothesis testing) was conducted using JMP® 16 Statistical software (SAS). Significance is given at the $\alpha=0.05$ level unless otherwise stated. Nonlinear regression was performed using the "specialized modeling" platform, "nonlinear." An empirical model was fitted to the isocratic elution kinetic data using the differential rate law-like equations. A model based on second order-like kinetics for product recovery given by [Equation 4] was chosen.

$$Y = \frac{Y_0 - Y_\infty}{1 + (Y_0 - Y_\infty)k_2 t} + Y_\infty, \quad \text{where } t_{Y_{1/2}} = \frac{1}{(Y_0 - Y_\infty)k_2}, \quad (4)$$

where Y is the recovery, Y_∞ is recovery as $t \rightarrow \infty$, Y_0 is recovery at $t=0$, k_2 is decay rate constant (min^{-1}), t is time (min), and $t_{Y_{1/2}}$ is recovery halving-time (min).

The gradient elution profiles demonstrated a two-peak profile comprised of a weaker binding leading peak (Peak 1) and a more strongly binding lagging peak (Peak 2). These profiles were assumed to represent two distinct subpopulations within the eluate, each of which could be approximated by a normal-like distribution with defined skew to account for the nonnormal behavior of the probability density function. Kurtosis was determined to be nonconsequential for both subpopulations as excess kurtosis was less than ± 2 across all timepoints (George & Mallery, 2010). The

overall concentration profile was defined as the additive effect of these two skewed-Gaussian populations, each representing a single peak in the elution profile (Equation 5a).

$$q_1 = \frac{B_1 \varphi(X_1) \cdot 2\Phi(\alpha_1 X_1)}{\Phi(0)} + \frac{B_2 \varphi(X_2) \cdot 2\Phi(\alpha_2 X_2)}{\Phi(0)}, \quad (5a)$$

where $\varphi(X)$ is the normal distribution probability density function and $\Phi(X)$ is normal cumulative distribution function defined by:

$$\varphi(X) = \frac{1}{s_1 \sqrt{2\pi}} e^{-\frac{X^2}{2}}, \quad (5b)$$

$$\Phi(X) = \frac{1}{2} \left[1 + \operatorname{erf} \left(\frac{X}{\sqrt{2}} \right) \right] \quad \text{given} \quad X = \frac{x - m}{s}, \quad (5c)$$

where q_1 is the eluted viral concentration ($\mu\text{g/mL}$), $B_{1,2}$ is Peak Magnitude Coefficient (μg), $s_{1,2}$ is peak 1/2 standard deviation (mL), $m_{1,2}$ is Peak 1/2 mean (mL), x is volume (mL), $\alpha_{1,2}$ is skewness factor and $\Phi(0)$ is cumulative distribution function at $\alpha_{1,2} = 0$.

3 | RESULTS AND DISCUSSION

3.1 | The impact of time spent in the adsorbed state on functional and total LV recovery

An LV loss mechanism was hypothesized wherein adsorbed vector undergoes a conformational change from a reversibly bound to an irreversibly bound state, due to spreading and deformation of LV over the adsorbent surface. As such, a time-dependent nature to product recovery should be observed as the proportion of irreversibly bound material increases (Figure 1b).

Initial studies were performed to establish any impact of adsorption time on recovery as this has not been reported for LV. Turnbull et al. (2019) demonstrated high recovery of Ad5 vector over Nanofiber-Q adsorbents at 4 min adsorption time with losses of nearly 50% occurring within the first 24 min at high adsorbent ligand density. Adsorbed contact times of 5, 35, and 65 min were therefore chosen as a similar range that also covered common processing times, and practical constraints such as flowrates and sample collection times, within commercial LV manufacture. We conducted a DBC study and measured the point at which the first breakthrough of vector was observed in the flowthrough (DBC_{0%}) at 300 CV (data not shown, see Section 2.2). To achieve 5 min adsorption time membranes were underloaded at high flowrate using 95 CV of thawed CCH at 65 CV/min. This was followed by a 30 CV wash with Buffer A and elution using Buffer C at a reduced flowrate of 3 CV/min to completely elute product in 15 CV. To achieve extended adsorption periods, an additional 30 and 60 min static “on-column” incubation was implemented. Other authors previously investigated the impact of adsorbed contact time by manipulating flowrates or wash duration (Haimer et al., 2007; Turnbull et al., 2019; Ueberbacher et al., 2008). Due to the possibility of differing flowrates impacting the degree of particle entrapment or loss of LV infectivity due to shear damage, we

chose static incubations instead (Trilisky & Lenhoff, 2009). A representative chromatogram for the 5 and 65 min time points are shown (Figure 2a,b).

Initially “on-column” incubations were conducted in CCH at the end of loading (Figure 2b). This condition was chosen as the most relevant adsorption environment to industrial LV chromatography where CCH is typically loaded directly onto AIEX after clarification. However, under this condition the contacting mobile phase contains unbound media components and cell derived impurities such as proteases that could affect “on-column” stability. Experiments were therefore repeated with incubations conducted following the Buffer A wash to remove impurities from the “on-column” mobile phase. Both incubation hold points are indicated in Figure 2b.

Figure 2c,d shows the recovery of both functional titer and total particles. A marked difference in functional titer recovery was observed between the 5 and 35 min time points, with limited further impact observed at 65 min. Increasing the contact time from 5 to 65 min led to a reduction in TU recovery from 28% to 12% for the CCH mobile phase and from 33% to 10% for the Buffer A mobile phase. No functional titer was observed in the flowthrough, as expected from the DBC_{0%}. As a control, no impact on TU recovery was observed when CCH was incubated under ambient conditions outside the chromatography system on the bench for 65 min (TU recovery = 98%, data not shown). A further control was conducted to test for any loss of functionality that may result from the high flow environment experienced during loading. Twenty milliliters of CCH was pumped through the ÄKTA system at 65 mL/min without an AIEX membrane attached (0.75 mm diameter column tubing, $N = 3$ biological replicates). Although a small reduction in functional titer was observed (TU recovery = $85 \pm 3\%$, data not shown), the use of static incubations meant any small shear related losses could only occur during the initial loading phase. As the loading conditions were ubiquitous across all measured contact times, this decoupled the effect of shear from adsorption time loss measurements.

A similar contact time impact was observed for total particle recovery (Figure 2d) with a reduction from 27% to 12% and 31% to 10% for the CCH and Buffer A contacting mobile phases, respectively. Contacting mobile phase did not substantially impact the recovery of functional or total vector particles. As long-term functional vector stability was not significantly impacted by mobile phase (p -value = 0.515 at $t = 65$ min), this implies that the presence of media impurities does not considerably impact “on-column” losses. These data thus demonstrate that adsorbed contact time is a key factor influencing the recovery of both functional and total LV particles.

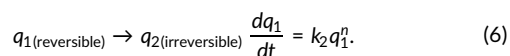
3.2 | Kinetics of LV loss with time spent in the adsorbed state

To gain a more detailed understanding of vector loss kinetics, additional 12.5 and 20 min time points were included for the Buffer A hold point to generate kinetic profiles. For HIV-1-GFP1 these were

conducted at $N = 2$ biological replicates due to material limitations. We also evaluated the effects of adsorbed contact time on a clinical vector encoding an onco-therapeutic CAR transgene. Some clinical transgenes (e.g., CAR) are membrane proteins, which during production can incorporate into the envelope of the LVs during budding, thereby altering the surface environment of the LV compared with vectors expressing a nonmembrane protein. Different transgenes can also have varying levels of cytotoxicity, from none to severely cytotoxic, which can influence differences in impurity content and vector production (Maunder et al., 2017). These factors may impact adsorption-related losses.

Experiments were therefore carried out for HIV-1-CAR vector but with an increased range of “on-column” incubation times, measuring up to 120 min. A substantial amount of total loaded p24 ($12 \pm 2\%$ - GFP1, $51 \pm 4\%$ - CAR) was detected in the AIEX flowthrough. HIV-1-based LVs have a core protein called p24 that would be inside an LV particle but can also be free in the supernatant from damaged vector particles or from cells releasing p24. As soluble p24 protein interacts weakly at pH 7.2, due to having an isoelectric point of pH 6.7, we assume this p24 was not vector-associated (Ehrlich et al., 2001; Zheng et al., 2012). This assumption was supported by functional titer, where no functional vector (TU) was detected in the flowthrough, and by DLS where we observed no particles in the 80–120 nm size range (data not shown). Thus, only the recovery of bound p24 was considered when measuring total particle recovery.

Figure 3a,b shows the loss kinetics of functional and total vector particles for both GFP- and CAR-expressing vectors. Previously, the rate of structural changes from the native to an unfolded or “spread” state of a protein on an adsorbent surface was shown to be proportional to the amount of protein bound in the native state and the free surface available, which was also a function of bound protein concentration (Snopok & Kostyukevich, 2006). This complex adsorption process could be likened to an irreversible reaction where native (reversibly bound) vector transitions to an irreversibly bound vector state. This irreversible binding depends on the concentration of reversibly bound vector or “reactant,” as shown below:



Thus, although not a true reaction rate description as this would detail a change in substrate concentration with time, the reduction in LV recovery (Y) followed the same trend as that of substrate concentration in a reaction rate model. We, therefore, inferred that a similar model structure would be suitable to describe this phenomenon. The initial substrate concentration in the reaction rate model could be likened to the maximum recovery value from the column (Y_0). We further adapted this description to include a final nonzero residual recovery value, Y_∞ , to characterize this observation in our data. The effective recovery range is thus defined as the difference between the maximum and residual recovery value, ($Y_0 - Y_\infty$). This adapted form of the differential rate equation was used to determine zero ($n = 0$), first ($n = 1$), and second ($n = 2$) order-like kinetics of reversibly bound vector, that is, eluted vector recovery. An equation

based on second order-like kinetics yielded the best empirical fit and was selected (Equation 4). An important parameter for analysis of this system is the time taken for recovery to fall to half of the effective recovery range, which we define as the recovery halving-time, $t_{Y_{1/2}}$, (Equation 4). This rate law like model was successful at describing the kinetics of both total and functional vector particles ($R^2 = 0.96$ and 0.94 , respectively) for HIV-1-GFP1 (Figure 3a,e) and HIV-1-CAR ($R^2 = 0.96$ and 0.88 , respectively) (Figure 3b,e).

For the therapeutic HIV-1-CAR a reduction in functional recovery from 49% at $t = 5$ min to 21% at $t = 140$ min was observed with similar profiles obtained for both total and functional vector particles, reporting a recovery halving-time of $t_{Y_{1/2}} = 14.2$ and 12.7 min respectively ($k_{2(p24)} = 1.14 \times 10^{-3}$ and $k_{2(TU)} = 1.74 \times 10^{-3} \text{ min}^{-1}$). This highlights the rapid rate of vector loss with over half of recoverable product lost within 15 min of adsorption. These data also demonstrate that reduction in functional and total particle recovery occurs at equivalent rates, implying material is lost due to physical retention on the membrane and not to deactivation of eluted LV (e.g., damage to viral envelope or rupture of the virion) as functional vector loss would occur faster in that case. This is supported by the relative activity data (Figure 3c) where no significant correlation between adsorbed contact time and relative activity was shown. When coupled with the significant increase in 0.5 M NaOH strip peak area (Figure 2a,b), these data strongly indicate recovery loss from increased irreversible binding.

Similar decay rates were seen for HIV-1-GFP1 functional titer with a recovery halving-time of $t_{Y_{1/2}} = 18.7$ min ($k_{2(TU)} = 1.14 \times 10^{-3} \text{ min}^{-1}$). However, the overall recovery values were generally lower for HIV-1-GFP with a maximum TU recovery of 33% at $t = 5$ min. The reasons for these differences between vector types is unclear, however, it could be down to the difference in membrane protein composition from CAR transgene protein being on the vector particles or transgene cytotoxicity causing difference in upstream production and inherent vector stability. For HIV-1-GFP1 we observed a higher total particle decay constant of $k_{2(p24)} = 3.20 \times 10^{-3} \text{ min}^{-1}$ which could result from defective particles undergoing conformational change faster than functional. However, due to the similarity between functional and total particle recoveries at most time points, this difference is likely due to an outlier at the $t = 20$ min time point where both data points were located below the 95% confidence band for the decay curve. This is further supported by the relative activity data (Figure 3c) where, like HIV-1-CAR, no significant trend was observed indicating loss due to an increase in the degree of irreversible binding. To confirm our time-dependent sorption behavior was specific to vector and not present in a smaller and more structurally rigid target, the concentration of eluted DNA was measured. Figure 3d shows eluted DNA was not correlated with adsorption time which reinforces our hypothesis that losses are vector-specific and due to the large size and lability of LVs. Furthermore, as no change in residual DNA or activity was observed, time spent in the adsorbed state does not appear to impact product quality with reduced times likely leading to improved DNA impurity profiles due to the higher vector to DNA ratio.

Despite a two- to threefold increase in vector recovery at $t = 5$ min as compared with $t = 65$ min, a maximum functional vector recovery of only 33% (HIV-1-GFP1) and 49% (HIV-1-CAR) was achieved. This may be due to other loss mechanisms such as physical entrapment of vector within the membranes complex internal structure at high flowrates (see Section 3.4), or a subpopulation of LV that is more susceptible to irreversible binding. Furthermore, we initially anticipated our recovery value would tend to zero at prolonged adsorption time as all vector is eventually lost to the irreversibly bound state, q_2 (Figure 1b). However, the presence of a plateau value in recovery ($Y_{\infty} = 2.8 - 16.3\%$) may suggest an LV subpopulation with reduced susceptibility to irreversible binding. Nevertheless, the models applied here are effective at describing reduction in LV recovery with time spent in the adsorbed state and highlight the rapid rate of product loss experienced. This emphasizes the need for considering time spent in the adsorbed state when designing high-recovery AIEX strategies.

3.3 | LV binding heterogeneity and the “two peak” profile

LV has previously been shown to elute over AIEX adsorbents in two “peaks” during linear gradient elution (Valkama et al., 2020; Yamada et al., 2003). Unlike other viral vector systems where dual peak profiles can be due to empty capsids, both these peaks contain

functionally active vector. Material detected in these peaks may have differences in structure or stability that impact contact time-related losses, as is the case for proteins during HIC where adiabatic compressibility and binding strength impact recovery loss (Roberts & Carta, 2022; Ueberbacher et al., 2008). We wished to assess the impact of adsorption time on vector eluted at different NaCl concentrations and whether peak 1 and peak 2 differed in their rate of loss to the irreversibly bound state.

A linear gradient elution (150–1350 mM NaCl) was conducted with representative elution chromatograms for 5 and 140 min incubation times given alongside a comparison of average peak areas in Figure 4. Increased adsorption time led to a reduction of elution UV-peak area alongside a substantial increase in the 0.5 M NaOH strip peak area (Figure 4c). These data agree with Figure 2, which also demonstrated a large increase in overall NaOH strip area likely from a growing proportion of irreversibly bound vector. There is a slight discrepancy between material lost in elution and gained in the NaOH strip, which may arise from a certain proportion of material remaining “on-column” after the strip.

Total and functional particle concentration was plotted against NaCl elution concentration (Figure 5a,b). A “two peak” elution profile comprising of a weakly binding “peak 1” (~450 mM NaCl) and a strongly binding “peak 2” (~950 mM NaCl) was observed in both cases and is generally consistent with those reported by Yamada et al. (2003). Physically, these two peaks could represent either LV that interact predominantly through the lipid envelope and those that

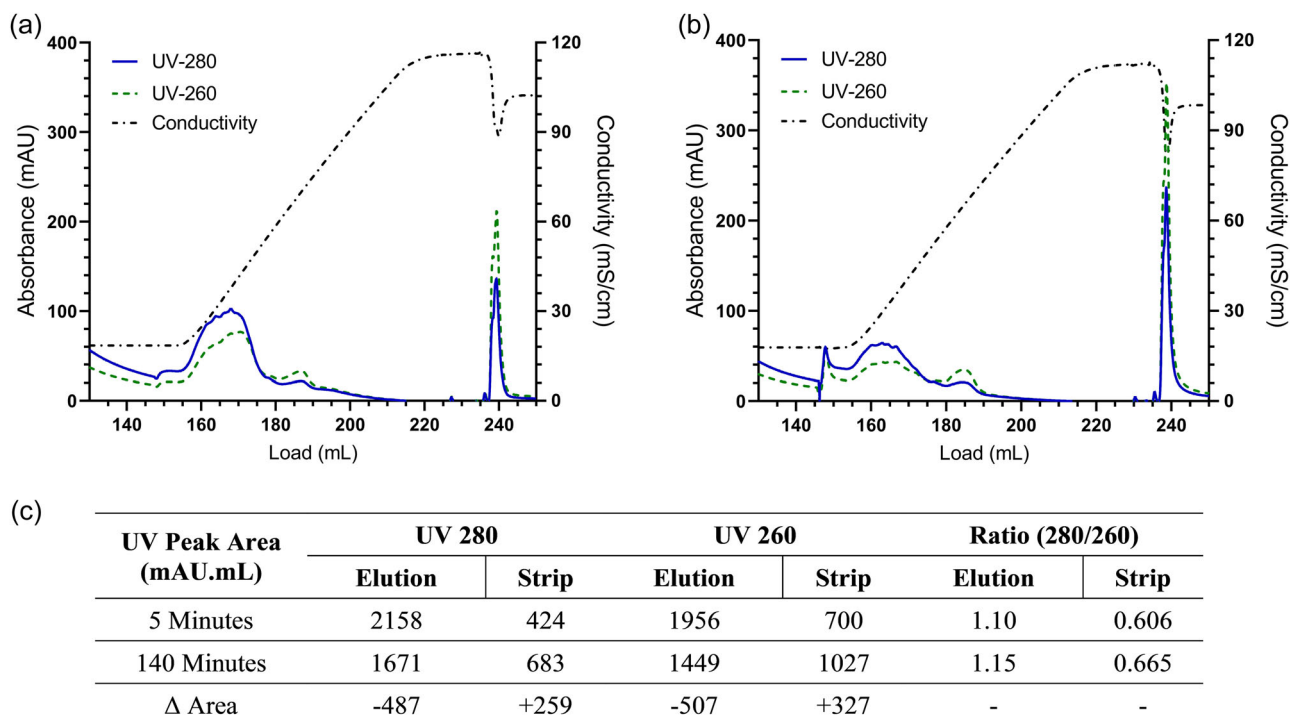


FIGURE 4 Representative chromatogram data for contact time gradient elution analysis demonstrating the increase in 0.5 M NaOH strip (final peak) area. (a) Elution profile of the 5-min adsorbed contact time chromatogram (b) Elution profile of the 140 min adsorbed contact time chromatogram (c) Table indicating the UV peak areas and relative change of elution and strip peaks between the 5 and 140 min contact time points.

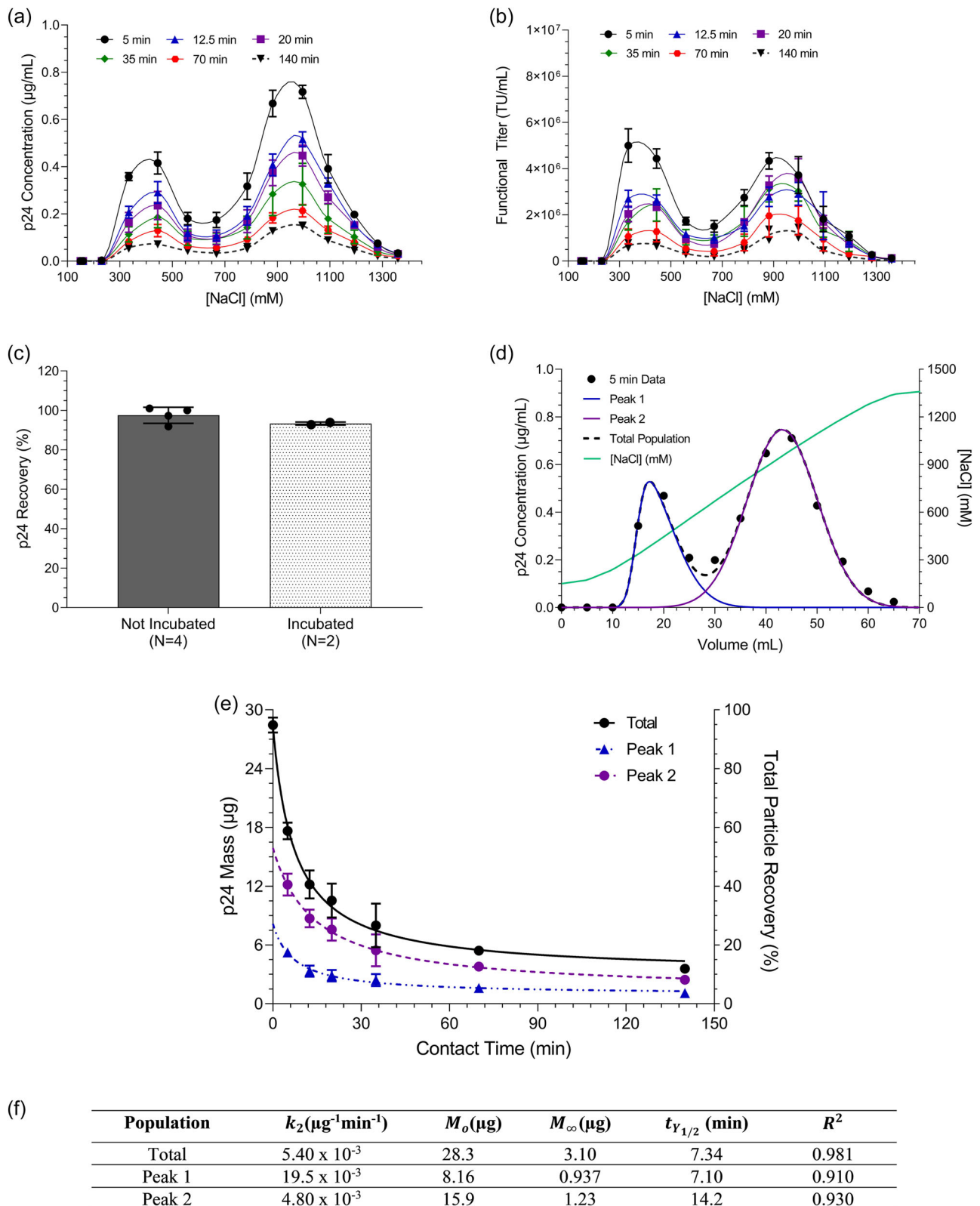


FIGURE 5 NaCl gradient elution analysis of GFP2 material over Q-membranes. Error bars represent 1 SD at $N = 3$ biological replicates. Individual runs are given for $t = 140$ min as this was conducted in biological duplicate due to material constraints. (a) p24 concentration as a function of elution NaCl concentration, a smoothing spline was applied to generate continuous profiles (b) Functional titer as a function of elution NaCl concentration, a smoothing spline was applied to generate continuous profiles (c) Impact of nonbinding conditions on p24 recovery. Biological replicates are indicated on figure. (d) Example deconstruction of the p24 elution profile into two separate skewed-Gaussian populations for the 5 min incubation time point. Overall elution profile is the sum of the two populations (e) Second order-like kinetic model fit to p24 mass of individual elution peaks as calculated from the skewed-Gaussian distribution parameters B_1 and B_2 . Corresponding total particle recovery is indicated on the right y-axis (f) Model fit parameters for individual peak profiles.

interact via avidity of surface proteins or simply two separate populations of LV with two distinct binding domains. Rodrigues et al. (2008) enzymatically removed envelope proteins from retrovirus and demonstrated elution occurred at a reduced conductivity (13.7–30 mS/cm), likely due to lipid membrane interaction which is comparable to our “peak 1” (21–49 mS/cm) (Rodrigues et al., 2008). Peak 1 may therefore represent interaction with the membrane itself and peak 2 with envelope protein. Differences in binding mode could arise from variations in the accessibility of envelope proteins and membrane. Subpopulations of LV with overall lower protein density may reside in peak 1 due to greater accessibility of the lipid bilayer. Wild-Type HIV-1 has been shown to display maturation dependent envelope clustering (Chojnacki et al., 2017). As such vector maturation state could impact envelope protein arrangement and expression. More generally, previous authors have demonstrated that significant variability in LV morphology is present during production, the extent of which was influenced by time after transfection (Desmaris et al., 2001).

3.4 | Total particle recovery under nonbinding conditions

To test whether particle entrapment phenomena significantly impacted LV recovery, six runs were conducted under nonbinding conditions by loading 95 CV of CCH spiked to 1350 mM NaCl onto the Q-membranes at 65 CV/min (Figure 5c). For two of these runs, a 15-min static incubation was implemented to see whether any additional recovery of entrapped particle occurred via diffusion back to bulk, as was observed in porous media (Trilisky & Lenhoff, 2009). An average total particle recovery (as measured by p24 capsid protein ELISA) of 96% was obtained for all nonbinding experiments with no substantial difference observed between incubated and non-incubated conditions (93% and 98%, respectively). Figure 5c shows minimal entrapment occurred within the Q-membranes suggesting it is not a considerable mechanism impacting LV recovery. This further implies that as 1350 mM NaCl is enough salt to completely disrupt the interaction with ALEX ligands, the major cause of LV loss is related to the binding process. These data could imply 96% recovery is attainable at $t = 0$ min, however, there may be a subpopulation of LV that is extremely susceptible to irreversible binding and once an interaction is formed cannot be recovered.

3.5 | The impact of time spent in the adsorbed state on eluted subpopulations

To determine the overall reduction in total particles of the two elution peaks in Figure 5a separately, we assumed these peaks were comprised of two subpopulations of vector present in the starting material before column load. While an initial assumption of the suitability of Gaussian probability distributions was made for the data, an improved fit was calculated when two distinct skewed

Gaussian probability density functions were additively employed (Equation 5a) to describe the behavior of the elution profile (Figure 5d). This model was then used to determine the model parameters to calculate the overall p24 mass in each peak (represented by B_1 and B_2) and plotted against contact time (Figure 5e). Figure 5e shows the kinetic profile of the individual peak mass as calculated from our Gaussian magnitude coefficients. The second order-like rate equation (used previously in Figure 3a,b) was then fit to the mass data in Figure 5e to describe the kinetics of total particle loss in peak 1 and peak 2 individually. The mass of the total population was calculated as the sum of the mass from all eluted fractions at each time point, with flow-through mass from the nonbinding study used to represent $t = 0$ min. Functional titer was not modeled in this way as the high salt environment present in peak 2 likely caused significant functionality loss before titer measurement thus biasing loss rate calculation.

Our initial hypothesis was that Y_∞ values resulted from a structurally resistant subpopulation of LV. These data demonstrate that no such resistance was observed in peak 1 and 2 with the eluted mass of both peaks impacted by adsorption time, reporting halving-times of $t_{Y_{1/2}} = 7.10$ and 14.2 min respectively ($k_2 = 19.5 \times 10^{-3} \mu\text{g}^{-1} \text{min}^{-1}$ and $k_2 = 4.80 \times 10^{-3} \mu\text{g}^{-1} \text{min}^{-1}$). Y_∞ values were also present in both peaks. However, there still may be subpopulations of LV contained in both peak 1 and peak 2 that are structurally resistant to contact time effects due to other reasons not measurable by techniques used here.

The peak 1 and 2 halving-times of $t_{Y_{1/2}} = 7.10$ min and $t_{Y_{1/2}} = 14.2$ min demonstrate a twofold higher rate of material loss in our weaker binding population (peak 1). This is somewhat unexpected as we anticipated that increased interaction strength would result in higher rate of material loss, as is typically observed in interactions with simple proteins. This could suggest that LV structure and inherent stability play a greater role in defining “on-column” losses than net charge. However, as our Peak 1 mean occurred at 430 mM NaCl, most of this population still interacts strongly with ALEX ligands. The increased interaction strength seen in peak 2 may have limited further impact to contact time driven losses. Manipulating mobile phase composition or adsorbent surface charge may provide a more effective tool for measuring reduced LV interaction strength as reported by Turnbull et al., 2019 for Ad5.

4 | CONCLUSION

The results of this work demonstrate that time spent in the adsorbed state is a critical factor impacting the recovery of both total and functional LV particles over ALEX Q-membrane adsorbents. We adopted a model based on second order-like kinetics to characterize our recovery profiles, demonstrating the recovery halving-time of functional LV encoding two separate transgenes (GFP and CAR) was in the range of 13–19 min. By measuring the relative activity of eluted material, and NaOH strip content, we demonstrate that vector loss stems from an increase in the degree of irreversible binding and not inactivation of eluted material. Experiments

under nonbinding conditions showed no significant LV loss (96% total particle recovery) thus ruling out particle entrapment as a notable loss process in this adsorbent.

We further characterized the role of LV binding heterogeneity by gradient elution, measuring a characteristic two-peak profile with an increased rate of loss in a weakly binding elution peak 1. This implies that LV structure plays a role in adsorption time-based losses. The specific mechanism that causes this irreversible binding remains unknown, however, one hypothesis is that this results from increasing interaction strength due to an increased area of contact (and thus multipoint attachment) caused by some conformational change of the vector in the bound state. One possibility is that it results from a spreading of the vector as it is pulled onto the surface, effectively “stretching” it over the adsorbent (Figure 1b). Alternatively, there may be specific adsorbent structural factors that give rise to this time-dependent recovery. Application of ligand functionalized polymers grafted to the membrane surface, present in the Q-membranes used here, has been suggested to display complex multistate binding in protein systems as the polymer tentacle gradually wraps around the protein (Diedrich et al., 2017; Nestola et al., 2014). Similar phenomena may be present in LV AIEX systems where tentacled polymer ligands are able to increase multipoint attachment with time due to their flexible and dynamic structure.

Adsorbent design characteristics, physiochemical conditions, and vector components may therefore all impact contact time effects. Determining which of these variables impact the parameters of the recovery equation (namely Y_0 , Y_∞ and the decay rate constant, k_2) is an important area for further investigation to identify factors that minimize the degree of adsorption time-based losses. We recommend that “on-column” stability data is incorporated into LV AIEX process development workflows as this will heavily influence the manufacturability of vector product.

This work has relevance for industrial manufacturing of CAR-T and other LV products, which typically do not consider time-dependent losses, but also in the wider viral vector chromatography field as rapid flow or rapid cycling technologies may be required to minimize processing time and thus boost vector recovery. The nature and cause of the “two peak” elution profile remains a focus of future work as more study is required to identify the key vector components responsible for binding LV to AIEX ligands.

AUTHOR CONTRIBUTIONS

Daniel G. Bracewell, Lee Davies, and George Pamenter conceived the study. George Pamenter designed and executed experiments and drafted the manuscript. Duygu Dikicioglu, Daniel G. Bracewell, and George Pamenter developed the analysis and modeling methodology. Research was performed in the laboratory of James Miskin, Kyriacos Mitrophanous, and Carol Knevelman. George Pamenter, Daniel G. Bracewell, Lee Davies, and Duygu Dikicioglu wrote the manuscript with contributions from all other authors.

ACKNOWLEDGMENTS

Collaboration and technical expertise from members of the Oxford Biomedica (UK) Ltd Process Research & Development department are

also thankfully acknowledged with specific recognition given to Dr Ciaran Lamont, Dr Francesca Liva, Miss Lydia Phipps, and Mr Thomas Williams. The research reported is affiliated with and supported by Oxford Biomedica (UK) Ltd. We thank the Engineering and Physical Sciences Research Council (EPSRC) for funding the Center for Doctoral Training in Bioprocess Engineering Leadership at UCL (Grant Ref: EP/S021868/1) and the Future Targeted Healthcare Manufacturing Hub in collaboration with UK universities and a consortium of industrial users and sector organizations (Grant Ref: EP/P006485/1).

CONFLICT OF INTEREST STATEMENT

The authors declare no conflict of interest.

DATA AVAILABILITY STATEMENT

Data may be available upon reasonable request to the author.

ORCID

George Pamenter  <http://orcid.org/0009-0009-9016-1716>

Duygu Dikicioglu  <http://orcid.org/0000-0002-3018-4790>

Daniel G. Bracewell  <http://orcid.org/0000-0003-3866-3304>

REFERENCES

- Alliance for Regenerative Medicine. (2022). *State of the Industry Briefing September 2022*. <http://alliancerm.org/wp-content/uploads/2022/10/ARM-H1-2022-R13.pdf>
- Bandeira, V., Peixoto, C., Rodrigues, A. F., Cruz, P. E., Alves, P. M., Coroadinha, A. S., & Carrondo, M. J. T. (2012). Downstream processing of lentiviral vectors: Releasing bottlenecks. *Human Gene Therapy Methods*, 23(4), 255–263. <https://doi.org/10.1089/hgtb.2012.059>
- Bulcha, J. T., Wang, Y., Ma, H., Tai, P. W. L., & Gao, G. (2021). Viral vector platforms within the gene therapy landscape. *Signal Transduction and Targeted Therapy*, 6(1), 53. <https://doi.org/10.1038/s41392-021-00487-6>
- Cell and Gene Therapy Catapult. (2022). *The Cell and Gene Therapy Catapult UK clinical trials database*. <https://ct.catapult.org.uk/resources/clinical-trials-database>
- Chojnacki, J., Waithe, D., Carravilla, P., Huarte, N., Galiani, S., Enderlein, J., & Eggeling, C. (2017). Envelope glycoprotein mobility on HIV-1 particles depends on the virus maturation state. *Nature Communications*, 8(1), 545. <https://doi.org/10.1038/s41467-017-00515-6>
- Desmaris, N., Bosch, A., Salaün, C., Petit, C., Prévost, M. C., Tordo, N., Perrin, P., Schwartz, O., de Rocquigny, H., & Heard, J. M. (2001). Production and neurotropism of lentivirus vectors pseudotyped with lyssavirus envelope glycoproteins. *Molecular Therapy*, 4(2), 149–156. <https://doi.org/10.1006/mthe.2001.0431>
- Diedrich, J., Heymann, W., Leweke, S., Hunt, S., Todd, R., Kunert, C., Johnson, W., & von Lieres, E. (2017). Multi-state steric mass action model and case study on complex high loading behavior of mAb on ion exchange tentacle resin. *Journal of Chromatography A*, 1525, 60–70. <https://doi.org/10.1016/j.chroma.2017.09.039>
- Ehrlich, L. S., Liu, T., Scarlata, S., Chu, B., & Carter, C. A. (2001). HIV-1 capsid protein forms spherical (immature-like) and tubular (mature-like) particles in vitro: Structure switching by pH-induced conformational changes. *Biophysical Journal*, 81(1), 586–594. [https://doi.org/10.1016/S0006-3495\(01\)75725-6](https://doi.org/10.1016/S0006-3495(01)75725-6)
- FDA. (2021, June 14). KYMRIAH (tisagenlecleucel). Product Information. <https://www.fda.gov/vaccines-blood-biologics/cellular-gene-therapy-products/kymriah-tisagenlecleucel>

- FDA. (2022a, March 21). CARVYKTI. Product Information. <https://www.fda.gov/vaccines-blood-biologics/carvykti>
- FDA. (2022b, August 17). FDA approves first cell-based gene therapy to treat adult and pediatric patients with beta-thalassemia who require regular blood transfusions. FDA News Release. <https://www.fda.gov/news-events/press-announcements/fda-approves-first-cell-based-gene-therapy-treat-adult-and-pediatric-patients-beta-thalassemia-who>
- George, D., & Mallery, P. (2010). *SPSS for Windows Step by Step: A Simple Guide and Reference*, 11.0 Update (10th ed.). Allyn and Bacon.
- Ghosh, R., Koley, S., Gopal, S., Rodrigues, A. L., Dordick, J. S., & Cramer, S. M. (2022). Evaluation of lentiviral vector stability and development of ion exchange purification processes. *Biotechnology Progress*, 38(6), e3286. <https://doi.org/10.1002/btpr.3286>
- Glover, C. (2021). *How to gear up for more stringent gene and cell therapy regulations*. European Pharmaceutical Manufacturer. <https://pharmaceuticalmanufacturer.media/pharmaceutical-industry-insights/biopharma-news/how-to-gear-up-for-more-stringent-gene-and-cell-therapy-regu/>
- Haimer, E., Tscheliessnig, A., Hahn, R., & Jungbauer, A. (2007). Hydrophobic interaction chromatography of proteins IV. *Journal of Chromatography A*, 1139(1), 84–94. <https://doi.org/10.1016/j.chroma.2006.11.003>
- Huang, Y., Bi, J., Zhou, W., Li, Y., Wang, Y., Ma, G., & Su, Z. (2006). Improving recovery of recombinant hepatitis B virus surface antigen by ion-exchange chromatographic supports with low ligand density. *Process Biochemistry*, 41(11), 2320–2326. <https://doi.org/10.1016/j.procbio.2006.06.004>
- Jungbauer, A., Machold, C., & Hahn, R. (2005). Hydrophobic interaction chromatography of proteins. *Journal of Chromatography A*, 1079(1–2 SPEC. ISS), 221–228. <https://doi.org/10.1016/j.chroma.2005.04.002>
- Khatwani, S. L., Pavlova, A., & Pirot, Z. (2021). Anion-exchange HPLC assay for separation and quantification of empty and full capsids in multiple adeno-associated virus serotypes. *Molecular Therapy - Methods & Clinical Development*, 21, 548–558. <https://doi.org/10.1016/j.omtm.2021.04.003>
- King, S. R. (1994). HIV: Virology and mechanisms of disease. *Annals of Emergency Medicine*, 24, 443–449.
- Ladd Effio, C., Hahn, T., Seiler, J., Oelmeier, S. A., Asen, I., Silberer, C., Villain, L., & Hubbuch, J. (2016). Modeling and simulation of anion-exchange membrane chromatography for purification of Sf9 insect cell-derived virus-like particles. *Journal of Chromatography A*, 1429, 142–154. <https://doi.org/10.1016/j.chroma.2015.12.006>
- Lewis, P., Hensel, M., & Emerman, M. (1992). Human immunodeficiency virus infection of cells arrested in the cell cycle. *The EMBO Journal*, 11(8), 3053–3058. <https://doi.org/10.1002/j.1460-2075.1992.tb05376.x>
- Mátrai, J., Chuah, M. K., & Vandendriessche, T. (2010). Recent advances in lentiviral vector development and applications. *Molecular Therapy*, 18(3), 477–490. <https://doi.org/10.1038/mt.2009.319>
- Maunder, H. E., Wright, J., Kolli, B. R., Vieira, C. R., Mkandawire, T. T., Tatoris, S., Kennedy, V., Iqbal, S., Devarajan, G., Ellis, S., Lad, Y., Clarkson, N. G., Mitrophanous, K. A., & Farley, D. C. (2017). Enhancing titres of therapeutic viral vectors using the transgene repression in vector production (TRiP) system. *Nature Communications*, 8, 14834. <https://doi.org/10.1038/ncomms14834>
- Merten, O. W., Hebben, M., & Bovolenta, C. (2016). Production of lentiviral vectors. *Molecular Therapy - Methods and Clinical Development*, 3, 16017. <https://doi.org/10.1038/mtm.2016.17>
- Moreira, A. S., Cavaco, D. G., Faria, T. Q., Alves, P. M., Carrondo, M. J. T., & Peixoto, C. (2021). Advances in Lentivirus Purification. *Biotechnology Journal*, 16(1), 2000019. <https://doi.org/10.1002/biot.202000019>
- Naldini, L., Blomer, U., Gallay, P., Ory, D., Mulligan, R., Gage, F. H., Verma, I. M., & Trono, D. (1996). *In Vivo Gene Delivery and Stable Transduction of Nondividing Cells by a Lentiviral Vector*. <https://www.science.org>
- Nestola, P., Villain, L., Peixoto, C., Martins, D. L., Alves, P. M., Carrondo, M. J. T., & Mota, J. P. B. (2014). Impact of grafting on the design of new membrane adsorbents for adenovirus purification. *Journal of Biotechnology*, 181, 1–11. <https://doi.org/10.1016/j.jbiotec.2014.04.003>
- Nguyen, D. H., & Hildreth, J. E. (2000). Evidence for budding of human immunodeficiency virus type 1 selectively from glycolipid-enriched membrane lipid rafts. *Journal of Virology*, 74(7), 3264–3272. <https://journals.asm.org/journal/jvi>
- National Cancer Institute, National Institutes of Health. (2022, March 1). *CAR T Cells: Engineering patients' immune cells to treat their cancers*. <https://www.cancer.gov/about-cancer/treatment/research/car-t-cells>
- Orr, V., Zhong, L., Moo-Young, M., & Chou, C. P. (2013). Recent advances in bioprocessing application of membrane chromatography. *Biotechnology Advances*, 31(4), 450–465. <https://doi.org/10.1016/j.biotechadv.2013.01.007>
- Roberts, J. A., & Carta, G. (2022). Protein adsorption and separation with monomodal and multimodal anion exchange chromatography resins. Part II. *Journal of Chemical Technology and Biotechnology*, 98, 357–368. <https://doi.org/10.1002/jctb.7247>
- Rodrigues, T., Alves, A., Lopes, A., Carrondo, M. J. T., Alves, P. M., & Cruz, P. E. (2008). Removal of envelope protein-free retroviral vectors by anion-exchange chromatography to improve product quality. *Journal of Separation Science*, 31(20), 3509–3518. <https://doi.org/10.1002/jssc.200800195>
- Ruscic, J., Perry, C., Mukhopadhyay, T., Takeuchi, Y., & Bracewell, D. G. (2019). Lentiviral vector purification using nanofiber ion-exchange chromatography. *Molecular Therapy - Methods & Clinical Development*, 15, 52–62. <https://doi.org/10.1016/j.omtm.2019.08.007>
- Snopok, B. A., & Kostyukevich, E. V. (2006). Kinetic studies of protein-surface interactions: A two-stage model of surface-induced protein transitions in adsorbed biofilms. *Analytical Biochemistry*, 348(2), 222–231. <https://doi.org/10.1016/j.ab.2005.11.009>
- Trilisky, E. I., & Lenhoff, A. M. (2009). Flow-dependent entrapment of large bioparticles in porous process media. *Biotechnology and Bioengineering*, 104(1), 127–133. <https://doi.org/10.1002/bit.22370>
- Turnbull, J., Wright, B., Green, N. K., Tarrant, R., Roberts, I., Hardick, O., & Bracewell, D. G. (2019). Adenovirus 5 recovery using nanofiber ion-exchange adsorbents. *Biotechnology and Bioengineering*, 116(7), 1698–1709. <https://doi.org/10.1002/bit.26972>
- Ueberbacher, R., Haimer, E., Hahn, R., & Jungbauer, A. (2008). Hydrophobic interaction chromatography of proteins. *Journal of Chromatography A*, 1198–1199(1–2), 154–163. <https://doi.org/10.1016/j.chroma.2008.05.062>
- Urabe, M., Xin, K. Q., Obara, Y., Nakakura, T., Mizukami, H., Kume, A., Okuda, K., & Ozawa, K. (2006). Removal of empty capsids from type 1 adeno-associated virus vector stocks by anion-exchange chromatography potentiates transgene expression. *Molecular Therapy*, 13(4), 823–828. <https://doi.org/10.1016/j.yjmt.2005.11.024>
- Valkama, A. J., Oruetebarria, I., Lipponen, E. M., Leinonen, H. M., Käyhty, P., Hynynen, H., Turkki, V., Malinen, J., Miinalainen, T., Heikura, T., Parker, N. R., Ylä-Herttua, S., & Lesch, H. P. (2020). Development of large-scale downstream processing for lentiviral vectors. *Molecular Therapy - Methods & Clinical Development*, 17, 717–730. <https://doi.org/10.1016/j.omtm.2020.03.025>
- Vicente, T., Fáber, R., Alves, P. M., Carrondo, M. J. T., & Mota, J. P. B. (2011). Impact of ligand density on the optimization of ion-exchange membrane chromatography for viral vector purification. *Biotechnology and Bioengineering*, 108(6), 1347–1359. <https://doi.org/10.1002/bit.23058>
- Vicente, T., Sousa, M. F. Q., Peixoto, C., Mota, J. P. B., Alves, P. M., & Carrondo, M. J. T. (2008). Anion-exchange membrane chromatography for purification of rotavirus-like particles. *Journal of Membrane*

- Science*, 311(1-2), 270–283. <https://doi.org/10.1016/j.memsci.2007.12.021>
- Yamada, K., McCarty, D. M., Madden, V. J., & Walsh, C. E. (2003). Lentivirus vector purification using anion exchange HPLC leads to improved gene transfer. *Biotechniques*, 34(5), 1074–1080. <https://doi.org/10.2144/03345dd04>
- Zheng, L., Jia, L., Li, B., Situ, B., Liu, Q., Wang, Q., & Gan, N. (2012). A sandwich HIV p24 amperometric immunosensor based on a direct gold electroplating-modified electrode. *Molecules*, 17(5), 5988–6000. <https://doi.org/10.3390/molecules17055988>

How to cite this article: Pamerter, G., Davies, L., Knevelman, C., Miskin, J., Mitrophanous, K., Dikicioglu, D., & Bracewell, D. G. (2023). Time-dependent sorption behavior of lentiviral vectors during anion-exchange chromatography. *Biotechnology and Bioengineering*, 120, 2269–2282. <https://doi.org/10.1002/bit.28483>